Applied Physics A (2021) 127:318
https://doi.org/10.1007/s00339-021-04435-7

Applied Physics A
Materials Science & Processing

Controlling the morphology of nanocrystalline $Y(OH)_3$ powders synthesized by microwave-hydrothermal route and effect of annealing

Thirupathi Gadipelly[1,4] · Arup Dasgupta[1] · D. Sornadurai[2] · Sandip Dhara[3]

Received: 12 January 2021 / Accepted: 11 March 2021 / Published online: 8 April 2021

Abstract

$Y(OH)_3$ is the main precursor material to inherit desirable morphologies for Y_2O_3. The $Y(OH)_3$ and Y_2O_3 are an important substitution for luminescent matrix and useful in temperature sensing applications. Nanostructured and phase-pure Y_2O_3 is also used as an essential dispersoid for the oxide dispersion strengthened steels which are candidate materials for future fast breeder reactors. In the present work, the nanostructured $Y(OH)_3$ is prepared indigenously by the microwave-hydrothermal route which is appropriate to provide-uniform heating to the material and the hydrothermal-pressure environment plays a major role in the growth kinetics of morphology. The synthesis was carried out at various microwave powers of 700 and 800 W to obtain the different morphologies of tubular and rod-like structures, respectively. The morphology is attributed to the influence of heat-rate on the variation in hydrothermal pressure governed by microwave power. The morphologies remain the same on calcination 800 °C. As-synthesized powder samples showed hexagonal structure whereas the cubic structure was observed for those calcined at 800 °C for both morphologies. The hydroxide vacancies lead to form a cubic structure that has a larger unit cell. The yttrium oxides showed lattice compaction for the rod-like structure but yttrium hydroxides did not depict any difference in the lattice for the tubular and rod-like morphologies. Likewise, Raman spectroscopy analysis confirmed the formation of hexagonal and cubic phases for the as-synthesized and calcined nanopowder samples, respectively.

Keywords Microwave hydrothermal synthesis · Crystal structure · Morphology · Raman spectroscopy · $Y(OH)_3$ · Y_2O_3

1 Introduction

The $Y(OH)_3$ and Y_2O_3 are significant for luminescent matrix and temperature sensing and catalytic applications [1–4]. The $Y(OH)_3$ is the main precursor material to inherit desirable morphologies for Y_2O_3. The nano-morphologies increase the scope in the field of nanotechnology [5–8]. Their structural, optical and electrical properties are made significant in engineering and technological fields [9–12]. Importantly, nanostructured Y_2O_3 dispersoids can occupy a smaller volume fraction in the metallic alloy matrix. This nanodispersion enhances strengthening properties of oxide dispersion strengthened (ODS) steels which are candidate materials for future fast breeder reactors. The Y_2O_3 material gives a wide range of temperature stability and good dispersion in ODS. So the challenges lie in the ability to produce optimal nano-oxide distributions in steel matrix to increase high-temperature stability along with resistance to excessive coarsening during the service or usage of the ODS steels [13]. These properties lead to superior high-temperature strength and irradiation tolerance [14]. The microwave-assisted synthesis route provides a localized steam atmosphere to the material in Teflon autoclave where the nucleation takes place in liquid to grow homogeneous and stable morphology over a conventional hydrothermal synthesis due to the typical heat transfer mechanism involved.

In this study, two microwave powers (700 and 800 W) were used to create hydrothermal pressure in the synthesis of $Y(OH)_3$. Two different morphologies (tube-like and

✉ Arup Dasgupta
arup@igcar.gov.in

1 Physical Metallurgy Division, Materials Metallurgy Group, Indira Gandhi Center for Atomic Research, HBNI, Kalpakkam 603102, India

2 Condensed Matter Physics Division, Indira Gandhi Center for Atomic Research, HBNI, Kalpakkam 603102, India

3 Surface and Nanoscience Division, Indira Gandhi Center for Atomic Research, HBNI, Kalpakkam 603102, India

4 Department of Physics, Basic Science and Humanities, Madanapalle Institute of Technology & Science, Madanapalli, Chittoor, Andhra Pradesh 517325, India

rod-like) were obtained for the powers. The powders were transformed into Y_2O_3 powders on calcination at 800 ºC. The morphologies were investigated by field emission scanning electron microscopy (FE-SEM) and transmission electron microscopy (TEM) to understand the growth kinetics. The structural phases were analyzed by X-ray diffraction (XRD) and Raman spectroscopy.

2 Materials and methods

2.1 Microwave hydrothermal synthesis

The $Y(OH)_3$ powder samples were obtained by the microwave-hydrothermal route at two microwave powers (700 and 800 W). The synthesis route was followed in a closed thick-walled Teflon autoclave similar to our earlier synthesis work [15]. The chemicals used for the growth of $Y(OH)_3$ were $Y(NO_3)_3$ (Sigma-Aldrich make, Assay 99.8%) and the NaOH (SRL make, Assay 98%). The Y_2O_3 samples were obtained by calcination of the hydroxides, respectively. The $Y(NO_3)_3$ was dissolved in demineralized water to get a uniform transparent solution. Then, 4 molar NaOH was added slowly to the chemical solution to reach a pH of 12. Then the solution was transferred into the Teflon autoclave under uniform stirring. That had been heated in a microwave oven for 150 s. The reaction for the synthesis of $Y(OH)_3$ powder samples was carried out at two microwave powers, 700 and 800 W. The estimated pressure and temperature were a maximum of 4 MPa and 260 °C [16–18]. The estimated heating rate is a maximum of 90 °C/min in the autoclave for the two different powers. The white precipitate was collected after the hydrothermal reaction and washed with deionized water. The as-synthesized powder was obtained after drying at 150 °C. This powder (hexagonal $Y(OH)_3$) had been calcined at 800 °C for 2 h to obtain the phase cubic nanostructured Y_2O_3.

2.2 Influence of synthesis conditions

Hydrothermal synthesis takes place at relatively low temperatures and high pressure (in the range of 10–40 atm). The heat transfer mechanism is very convenient in the microwave-hydrothermal route. The process allows the heating rate of 90 °C/min (for 90 ml solution) which is sufficiently higher compared to the rate of conventional hydrothermal route [19, 20]. The pressure hold time is controlled by the iterative application of specific microwave power at particular intervals. There is a strong influence on phase formation and morphology depending on the microwave power. If the synthesis conditions are optimized, this route can give desirable morphologies [21, 22]. The morphology can be modified without using any surfactants in this process. This route also has greater influences in manifesting the aspect ratio of various-shaped particles. $Y(OH)_3$ is the main precursor material to inherit various morphologies for cubic-Y_2O_3 which is usually derived by calcination of the hydroxide [23].

The chemical model is as follows for the synthesis followed by calcination:

$$2Y(NO_3)_3 + 6NaOH \rightarrow 2Y(OH)_3 \longrightarrow 2YOOH + H_2O \rightarrow Y_2O_3 + H_2O$$

The above equation explains that the as-synthesized composition (hexagonal-$Y(OH)_3$) transforms to monoclinic-YOOH at around 200 °C, the residual water content is expected to be evaporated between 200 and 500 °C, and cubic-Y_2O_3 is likely to form above 600 °C according to available literature [24, 25].

2.3 Characterization

The XRD patterns were recorded using an STOE X-ray diffractometer (STOE, Darmstadt, GmbH) operated in Bragg–Brentano geometry with Cu-Kα radiation. The diffracted X-ray was detected using a point detector attached along with a secondary monochromator. The detector made up of NaI: Tl scintillation crystal connected to a photomultiplier tube was used. The XRD patterns were analyzed by the Fullprof suite program. The micrographs were taken using FE-SEM (Zeiss sigma-300) and TEM (FEI make Tecnai G2 F30) operated at 200 kV. The Raman spectra of the specimens were recorded using the Raman spectrometer (inVia, Renishaw) equipped with 3000 grating and thermoelectric cooled CCD detector using excitation wavelength (λ_{exc}) of 532 nm.

3 Results and discussion

3.1 Morphological investigation

Figure 1 depicts the FE-SEM micrographs of tubular and rod-like nanostructures of $Y(OH)_3$ and Y_2O_3. The $Y(OH)_3$ powders (Fig. 1a, b) showed tubular and rod-like structures for the two microwave powers, 700 and 800 W, respectively. The Y_2O_3 powders (Fig. 1c, d) did not show changes in the morphology on the calcination of the hydroxides. In other words, the morphology of the Y_2O_3 powders followed that of

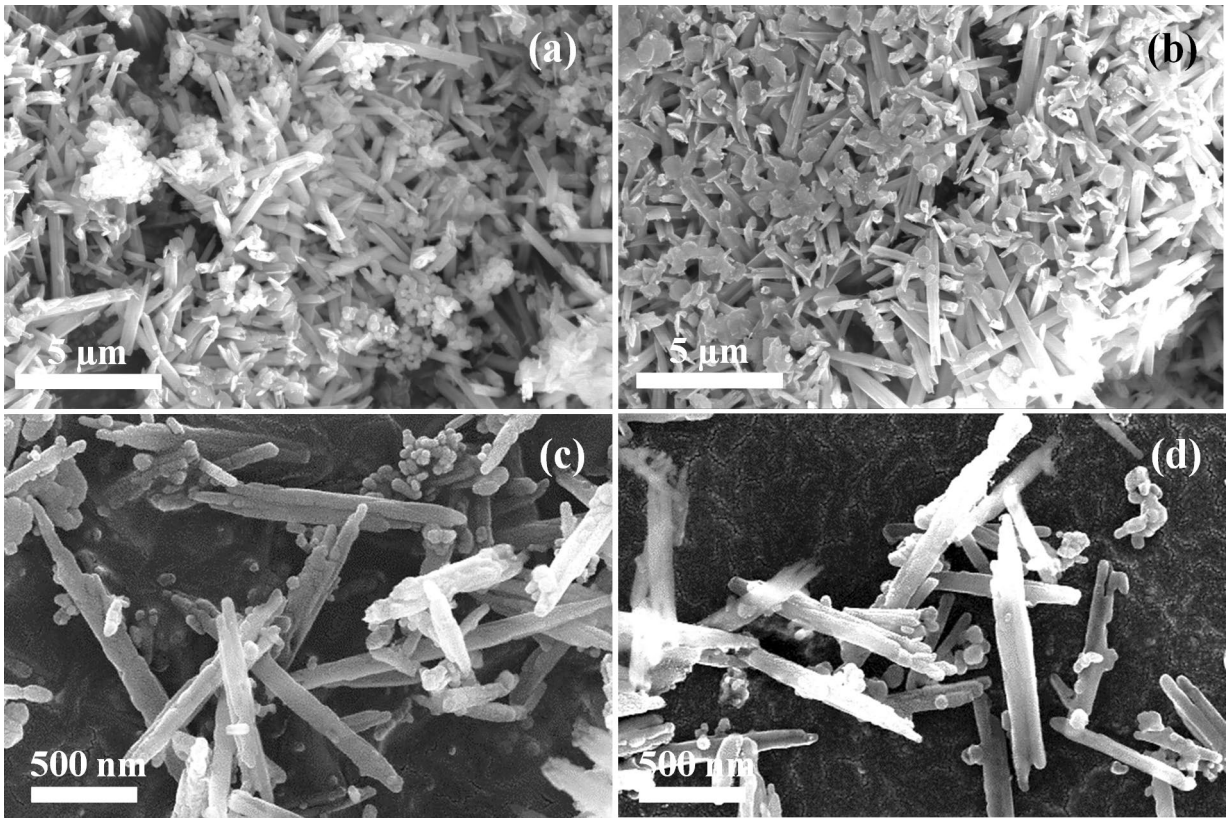

Fig. 1 SEM micrographs of nanostructures of $Y(OH)_3$: tubular (**a**) and rod-like (**c**) and Y_2O_3: tubular (**b**) and rod-like (**d**)

precursor $Y(OH)_3$. Studies on similar structured hydroxides said that the typical morphology was elongated hexagonal bipyramid or hexagonal-shaped rods for the hydrothermal synthesis when the growth was not controlled by surfactants [26]. There, the surfactant modified the surface thermodynamics of the material and supported the suitable morphology. However, the hydrothermal technique involved other important parameters to change the growth kinetics to obtain various morphologies [27, 28]. This was basically due to the way of introducing high hydrothermal energy to act on the surface of powder particles. When the hydrothermal pressure was created by microwaves in the autoclave, the thermal energy would be transferred to the particles from nearby water molecules. This process might support the formation of a uniform phase and influence the growth further [29]. Also, the morphology would grow along different crystal axes depending on the crystal structure of the material, the concentration of precursors, and hydrothermal pressure. The pressure would increase with temperature rapidly to a stable value. The low-pressure range could give spherical or hexagonal plate morphology for constant precursor concentration. The longer duration might affect the size of the particle morphology. The tubular and rod-like structures would appear in the range of high hydrothermal pressure. In the present work, the pressure used during the synthesis had been quite high. The rate of heating was dependent on the microwave power. That was different for the synthesis of both the hydroxides (700 and 800 W). So, both the morphologies (Fig. 1) were different by variation in the growth process. That could result in tubular and rod-like for the microwave powers of 700 and 800 W, respectively. A higher rate of heating could cause a faster increase in pressure where the duration was not sufficient to form a symmetric tubular structure and might be a case to stay in rod-like structures by changing the growth. The morphology (Fig. 1a, c) passed on to the oxides (Fig. 1b, d) when the hydroxides were calcined. The growth kinetics play a major role over crystallographic anisotropy which is attributed to the formation of rod-like structures [30, 31].

The length of tubes is governed by the hold-time of hydrothermal-pressure inside the autoclave. This is valid for the particular pressure range. The growth of tubes was

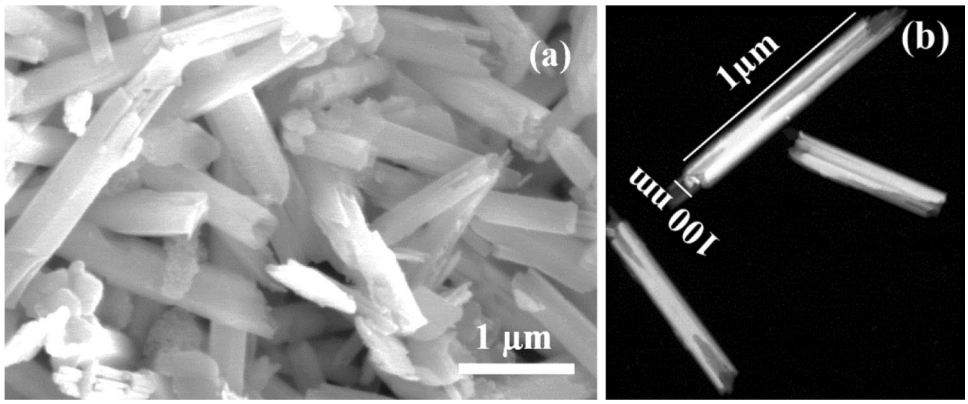

Fig. 2 **a** SEM and **b** TEM micrograph of tubular morphology $Y(OH)_3$

like hexagonal hollow rods when the images are zoomed. So magnified images of the tubular structure were presented for a better understanding of the tubular morphology. Figure 2 depicts the SEM and TEM micrograph of tubular morphology $Y(OH)_3$ in higher magnification, respectively. The tubular morphology consists of separable tubes in micron-sized length as shown in the SEM micrograph (Fig. 2a) [32, 33]. The TEM micrograph shows (Fig. 2b) the tubes broken along the length. It is expected that the pressure is too high to hold the tubular morphology. The growth mechanism is achieved to directly obtain rod-like morphology when the higher microwave power (800 W) is applied. This is attributed to the microwave power influence on the morphologies in hydrothermal synthesis.

3.2 XRD analysis

The Rietveld refinement was carried out to extract the crystallographic information of $Y(OH)_3$ and Y_2O_3 from the experimental XRD data. Figure 3 depicts the Rietveld refined XRD patterns of tubular and rod-like nanostructures of $Y(OH)_3$ and Y_2O_3. The hexagonal phase (space-group P63/m) was observed for the as-synthesized nanopowder of tubular and rod-like morphologies [34, 35]. The lattice parameters were $a = 6.2718(5)$ and $c = 3.5472(3)$ Å for the tubular, and $a = 6.2709(5)$ and $c = 3.5466(3)$ Å for the rod-like morphologies. Here, the parentheses represent the deviation at the last decimal place of lattice parameter values. A significant change is not observed in the XRD spectra of both $Y(OH)_3$ morphologies. This indicates the morphologies are influenced by the heating rate which is governed by the microwave power and there is only partial influence on the crystal structure of $Y(OH)_3$. Moreover, the manifestation of morphologies is related to the structural anisotropy of the hexagonal phase due to orientation in 1D geometry along the c-axis ((110)-orientation) [36]. A minor impurity phase was observed in a small fraction, left unindexed, which was intermediate impurity for both the hydroxides. The cubic-Y_2O_3 phase (space-group Ia-3) was observed for both calcined morphologies [37]. In other words, the $Y(OH)_3$ samples were transformed into cubic-Y_2O_3 at 800 °C. The lattice parameter values are $a = 10.6083(6)$ and $10.6035(6)$ Å for the tubular and rod-like structures, respectively, indicating lattice compaction in the rod-like structure compared to that for the tubular. This is attributed to the variation in lattice-density which is associated with bulk-density [38].

3.3 Raman spectra analysis

Raman spectroscopy was used to characterize the structural evolution of the hydroxide and oxide phases. Figure 4 depicts the Raman spectra of tubular and rod-like nanostructures of $Y(OH)_3$ and Y_2O_3. The observed phonon modes (Fig. 4a, b) supported the $Y(OH)_3$ formation in the given range. The major peaks, observed for tubular $Y(OH)_3$ at 316, 403, and 511 cm^{-1} (Fig. 4a, b), were assigned to A_g translatory, E_{2g} translatory, and E_{1g} liberation modes, respectively, corresponding to the Raman modes of $Y(OH)_3$. The Raman active vibrational modes are $4A_g$, $2E_{1g}$, and $5E_{2g}$ among the modes of $4A_g + 3B_g + 2E_{1g} + 5E_{2g} + 2A_u + 4B_u + 4E_{1u} + 2E_{2u}$ for hexagonal structure $Y(OH)_3$ having space group P63/m [39, 40]. Similarly, a major peak was observed at 377 cm^{-1} for tubular samples (Fig. 4c, d) corresponding to the A_g and T_g Raman modes among the expected 22 Raman active modes $4A_g + 4E_g + 14T_g$ for tubular Y_2O_3 [41–43]. This is attributed to the transformation of tubular-$Y(OH)_3$ to tubular-Y_2O_3 (Fig. 4a, c) in the given range. The property is observed to be similar for the Raman spectra of rod-like $Y(OH)_3$ and Y_2O_3 (Fig. 4b, d). The difference in peak

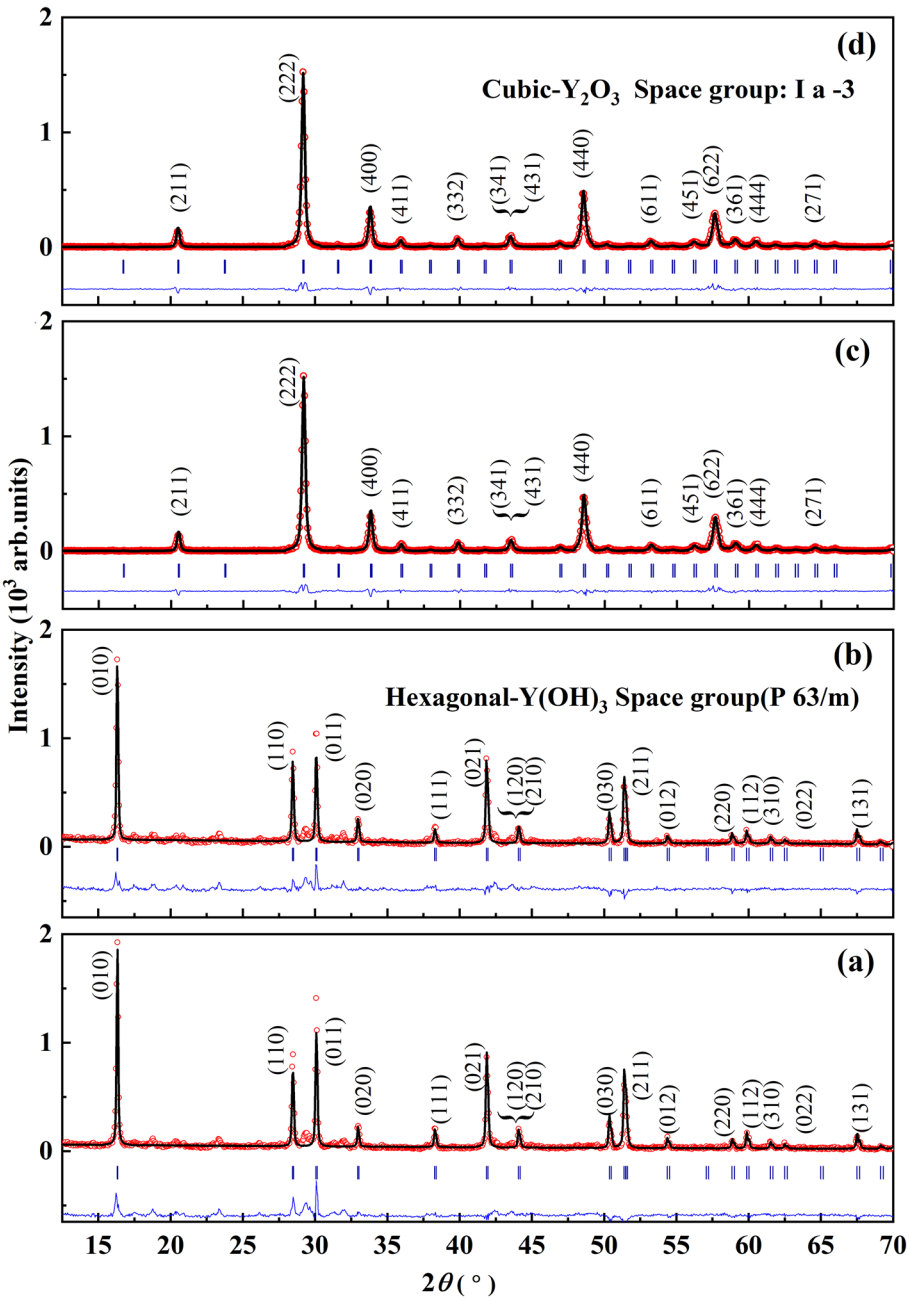

Fig. 3 Rietveld refined XRD patterns of nanostructures of $Y(OH)_3$: tubular (**a**) and rod-like (**b**) and Y_2O_3: tubular (**c**) and rod-like (**d**)

intensity may refer to crystal structures of $Y(OH)_3$ and Y_2O_3 for both morphologies. A minor variation of peak shift and broadening in the bands refers to the porosity and the average size of each phase having different morphologies and the Y_2O_3 inheriting the morphology from $Y(OH)_3$ on calcination.

4 Conclusions

The hydrothermal synthesis was carried out indigenously for nanostructured $Y(OH)_3$ at two microwave powers to obtain the morphologies, tubular and rod-like structure, attributing to the influence of heat-transfer mechanism on the variation in hydrothermal pressure governed by microwave power. The morphologies remained same on calcination but the

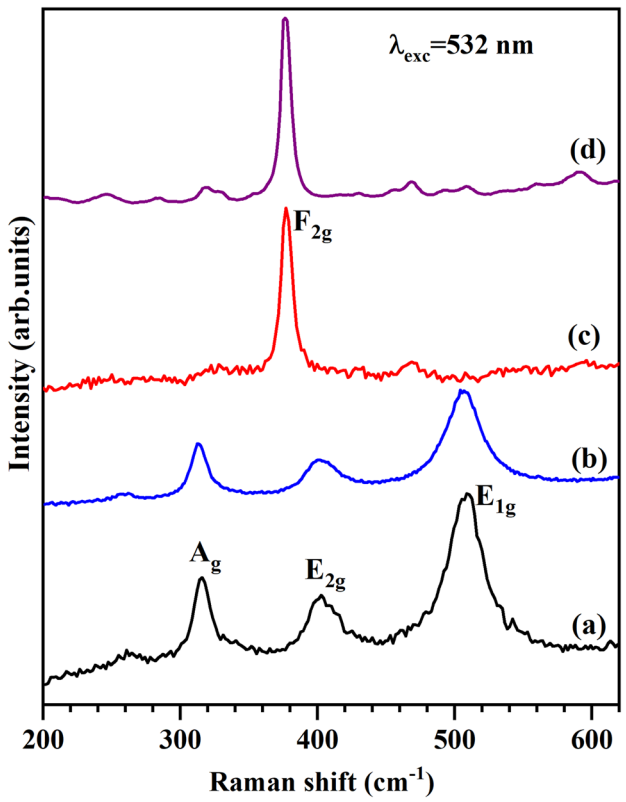

Fig. 4 Raman spectra of nanostructures of $Y(OH)_3$: tubular (**a**) and rod-like (**b**) and Y_2O_3: tubular (**c**) and rod-like (**d**)

crystal structure was transformed from hexagonal to cubic phase where the hydroxide vacancies lead to form a cubic structure that has a larger unit cell. The structural study was also supported by Raman spectroscopy. The formation of hydroxides is a base to obtain various morphologies for the oxides using various synthesis conditions.

Acknowledgements The authors are grateful to Dr. S. Raju, Associate Director-MMG for useful suggestions. The authors are also thankful for the support and encouragement provided by Dr. Shaju K Albert, Director, MMG, and the Director, IGCAR toward facilitating this work. One of the authors, Thirupathi, is grateful to IGCAR and MITS for financial support.

References

1. M. Yu, J. Su, G. Wang, Y. Li, Pt/Y2O3: Eu3+ composite nanotubes: Enhanced photoluminescence and application in dye-sensitized solar cells. Nano Res. **9**(8), 2338–2346 (2016). https://doi.org/10.1007/s12274-016-1120-z
2. G. Bilir, G. Ozen, J. Collins, B. Di Bartolo, Fabrication and spectral investigation of Y2O3:Nd3+ nanoparticles. Appl. Phys. A **115**(1), 263–273 (2014). https://doi.org/10.1007/s00339-013-7804-2
3. X. Cui, J. Lu, C. Gao, C. Hou, W. Wei, B. Peng, Luminescence properties of Nd3+-doped Y2O3 nanoparticles in organic media. Appl. Phys. A **103**(1), 27–32 (2011). https://doi.org/10.1007/s00339-010-6015-3
4. A. Kautsch, U. Brossmann, H. Krenn, F. Hofer, D.V. Szabó, R. Würschum, Structural and optical properties of nanoparticulate Y2O3: Eu2O3 made by microwave plasma synthesis. Appl. Phys. A **105**(3), 709–712 (2011). https://doi.org/10.1007/s00339-011-6589-4
5. A. García-Murillo, F.D.J. Carrillo-Romo, J. Oliva-Uc, T.A. Esquivel-Castro, S.D. de la Torre, Effects of Eu content on the luminescent properties of Y2O3: Eu3+ aerogels and Y(OH)3/Y2O3: Eu3+@SiO2 glassy aerogels. Ceram. Int. **43**(15), 12196–12204 (2017). https://doi.org/10.1016/j.ceramint.2017.06.079
6. X. Wnag, Y. Hu, X. Meng, Y. Li, M. Zhu, H. Jin, Synthesis of Y2O3 phosphor by a hydrolysis and oxidation method. J. Rare Earths **33**(7), 706–711 (2015). https://doi.org/10.1016/S1002-0721(14)60474-9
7. Y. Wu, W. Sun, X. Zhou, X. Jiao, J. Ding, Y. Li, Hydrothermal synthesis of Y(OH)3, Y(OH)3:Eu3+ nanotubes and the photoluminescence of Y(OH)3:Eu3+, Y2O3:Eu3+. J. Rare Earths **27**(5), 767–772 (2009). https://doi.org/10.1016/S1002-0721(08)60332-4
8. L.T.K. Giang et al., Preparation and characterization of yttrium hydroxide and oxide doped with rare earth ions (Eu3+, Tb3+) nano one-dimensional. Phys. Procedia **76**, 73–79 (2015). https://doi.org/10.1016/j.phpro.2015.10.014
9. M.K. Chong, K. Pita, C.H. Kam, Photoluminescence of sol–gel-derived Y2O3: Eu3+ thin-film phosphors with Mg2+ and Al3+ co-doping. Appl. Phys. A **79**(3), 433–437 (2004). https://doi.org/10.1007/s00339-004-2737-4
10. L.A. Diaz-Torres, P. Salas, J. Oliva, E. Resendiz-L, C. Rodriguez-Gonzalez, O. Meza, Tuning from green to red the upconversion emission of Y2O3:Er3+–Yb3+ nanophosphors. Appl. Phys. A **123**(1), 25 (2016). https://doi.org/10.1007/s00339-016-0668-5
11. D.J. Seo, Y.C. Kang, S.B. Park, The synthesis of (Y1-xGdx)2O3: Eu phosphor particles by flame spray pyrolysis with LiCl flux. Appl. Phys. A **77**(5), 659–663 (2003). https://doi.org/10.1007/s00339-002-1758-0
12. A.G. Ali, B.F. Dejene, H.C. Swart, Temperature dependence of structural and luminescence properties of Eu3+-doped Y2O3 red-emitting phosphor thin films by pulsed laser deposition. Appl. Phys. A **122**(4), 382 (2016). https://doi.org/10.1007/s00339-016-9946-5
13. P. Bhaskar, A. Dasgupta, M. Kamruddin, S. Saroja, Microstructural studies on Ti–Y2O3 interface reaction products. Trans. Indian Inst. Met. **69**(4), 901–905 (2016). https://doi.org/10.1007/s12666-015-0576-y
14. P.K. Parida, A. Dasgupta, K. Jayasankar, M. Kamruddin, S. Saroja, Structural studies of Y2O3 dispersoids during mechanical milling and annealing in a Fe-15 Y2O3 model ODS alloy. J. Nucl. Mater. **441**(1–3), 331–336 (2013). https://doi.org/10.1016/j.jnucmat.2013.06.016
15. T. Gadipelly et al., Synthesis and structural characterisation of Y2Ti2O7 using microwave hydrothermal route. J. Alloy. Compd. **814**, 152273 (2020). https://doi.org/10.1016/j.jallcom.2019.152273
16. S. Som, S. Das, C.-Y. Yang, C.-H. Lu, Microwave-assisted hydrothermal synthesis of Eu2O3-coated spherical Y2O3 ceramic particles. Ceram. Int. **42**(7), 8022–8029 (2016). https://doi.org/10.1016/j.ceramint.2016.01.208
17. S. Som et al., Synthesis of strong red emitting Y2O3:Eu3+ phosphor by potential chemical routes: comparative investigations on the structural evolutions, photometric properties and Judd–Ofelt analysis. RSC Adv. **5**(87), 70887–70898 (2015). https://doi.org/10.1039/C5RA13247A
18. A.J. Abdulghani, W.M. Al- Ogedy, Preparation and characterization of yttrium oxide nanoparticles at different calcination

temperatures from yttrium hydroxide prepared by hydrothermal and hydrothermal microwave methods. Iraqi J. Sci. **56**, 16 (2015)
19. B.K. Banik, D. Bandyopadhyay, *Advances in Microwave Chemistry* (CRC Press, 2018).
20. J. Kaszewski et al., Reduction of Tb4+ ions in luminescent Y2O3: Tb nanorods prepared by microwave hydrothermal method. J. Rare Earths **34**(8), 774–781 (2016). https://doi.org/10.1016/S1002-0721(16)60093-5
21. J. Kaszewski et al., Y2O3: Eu nanocrystals as biomarkers prepared by a microwave hydrothermal method. Opt. Mater. **59**, 157–164 (2016). https://doi.org/10.1016/j.optmat.2015.12.007
22. Y. Liu, Y. Ruan, L. Song, W. Dong, C. Li, Morphology-controlled synthesis of Y2O3:Eu3+ and the photoluminescence property. J. Alloy. Compd. **581**, 590–595 (2013). https://doi.org/10.1016/j.jallcom.2013.07.071
23. M. Ghaderi, R. Shoja Razavi, M.R. Loghman-Estarki, S. Ghorbani, Spark plasma sintering of transparent Y 2 O 3 ceramic using hydrothermal synthesized nanopowders. Ceram. Int. **42**(13), 14403–14410 (2016). https://doi.org/10.1016/j.ceramint.2016.06.022
24. B. Xu, G. Dong, J. Liu, K. Zou, D. Wang, The luminescence regulation effect of Na + on the Yb 3+ /Er 3+ co-doped Y 2 O 3 up-conversion films. J. Lumin. **203**, 16–25 (2018). https://doi.org/10.1016/j.jlumin.2018.05.051
25. M.S. de Almeida et al., Novel Gd(OH)3, GdOOH and Gd2O3 Nanorods: microwave-assisted hydrothermal synthesis and optical properties. Mater. Res. **19**(5), 1155–1161 (2016). https://doi.org/10.1590/1980-5373-MR-2016-0252
26. X. Ji, P. Hu, X. Li, L. Zhang, J. Sun, Hydrothermal control, characterization, growth mechanism, and photoluminescence properties of highly crystalline 1D Eu(OH) $_3$ nanostructures. RSC Adv. **10**(55), 33499–33508 (2020). https://doi.org/10.1039/D0RA04338A
27. Y. Zong, J. Feng, Y. Sun, X. Li, J. Bai, X. Zheng, Hydrothermal synthesis of uniform Fe-doped Gd(OH)3 nanorods and their magnetic properties: phase conversion from paramagnetism to ferromagnetism. Ceram. Int. **43**(10), 7881–7888 (2017). https://doi.org/10.1016/j.ceramint.2017.03.109
28. Z. Wen, C. Liang, H. Bi, Y. Li, R. Che, Controllable synthesis of elongated hexagonal bipyramid shaped La(OH)3 nanorods and the distribution of electric property by off-axis electron holography. Nano Res. **9**(9), 2561–2571 (2016). https://doi.org/10.1007/s12274-016-1142-6
29. Md.H. Zahir, T. Suzuki, Y. Fujishiro, M. Awano, Synthesis and characterization of Sm3+-doped Y(OH)3 and Y2O3 nanowires and their NO reduction activity. J. Alloy. Compd. **476**(1–2), 335–340 (2009). https://doi.org/10.1016/j.jallcom.2008.08.047
30. G. Li, Y. Liang, M. Zhang, D. Yu, Size-tunable synthesis and luminescent properties of Gd(OH)3: Eu3+ and Gd2O3: Eu3+ hexagonal nano-/microprisms. CrystEngComm **16**(29), 6670–6679 (2014)
31. Z. Huang et al., A new method for the preparation of transparent Y2O3 nanocrystalline ceramic with an average grain size of 20 nm. Scripta Mater. **182**, 57–61 (2020). https://doi.org/10.1016/j.scriptamat.2020.02.044
32. Y. Mao, J.Y. Huang, R. Ostroumov, K.L. Wang, J.P. Chang, Synthesis and luminescence properties of erbium-doped Y_2O_3 nanotubes. J Phys. Chem. C **112**(7), 2278–2285 (2008). https://doi.org/10.1021/jp0773738
33. X. Zhang et al., Shape-controlled synthesis and luminescence properties of yttria phosphors. CrystEngComm **13**(8), 3057 (2011). https://doi.org/10.1039/c0ce00887g
34. G. Chen, W. Qi, Y. Li, C. Yang, X. Zhao, Hydrothermal synthesis of Y2O3:Eu3+ nanorods and its growth mechanism and luminescence properties. J. Mater. Sci.: Mater. Electron. **27**(6), 5628–5634 (2016). https://doi.org/10.1007/s10854-016-4470-0
35. Z.S. Chen, W.P. Gong, T.F. Chen, S.L. Li, Synthesis and characterization of pyrochlore-type yttrium titanate nanoparticles by modified sol–gel method. Bull. Mater. Sci. **34**(3), 429–434 (2011). https://doi.org/10.1007/s12034-011-0116-2
36. N. Li, K. Yanagisawa, "Yttrium oxide nanowires",. Nanowires Sci. Technol. (2010). https://doi.org/10.5772/39501
37. C.-H. Yan, Z.-G. Yan, Y.-P. Du, J. Shen, C. Zhang, W. Feng, Chapter 251-controlled synthesis and properties of rare earth nanomaterials, in *Handbook on the physics and chemistry of rare earths*, vol. 41, ed. by K.A. Gschneidner, J.-C.G. Bünzli, V.K. Pecharsky, (Elsevier, 2011), pp. 275–472
38. J. Liu, W. Huang, Z. Xia, Y. Xu, Facile synthesis of accordion-like Y2O3:Er3+ nanothermometers for ratiometric temperature sensing applications. J. Lumin. **223**, 117207 (2020). https://doi.org/10.1016/j.jlumin.2020.117207
39. Q. Mu, Y. Wang, A simple method to prepare Ln(OH)3 (Ln=La, Sm, Tb, Eu, and Gd) nanorods using CTAB micelle solution and their room temperature photoluminescence properties. J. Alloy. Compd. **509**(5), 2060–2065 (2011). https://doi.org/10.1016/j.jallcom.2010.10.141
40. J.-G. Kang, B.-K. Min, Y. Sohn, Synthesis and characterization of Gd(OH)3 and Gd2O3 nanorods. Ceram. Int. **41**(1), 1243–1248 (2015). https://doi.org/10.1016/j.ceramint.2014.09.053
41. D. Richard, M. Rentería, A.W. Carbonari, M. Romero, R. Faccio, Preparation of In-doped Y2O3 ceramics through a sol-gel process: Effects on the structural and electronic properties. Ceram. Int. **46**(10), 16088–16095 (2020). https://doi.org/10.1016/j.ceramint.2020.03.161
42. S. Kalaivani, A. Guleria, D. Kumar, S. Kannan, Bulk yttria as a host for lanthanides in biomedical applications: influence of concentration gradients on structural, mechanical, optical, and in vitro imaging behavior. ACS Appl. Bio Mater. **2**(10), 4634–4647 (2019). https://doi.org/10.1021/acsabm.9b00718
43. P. Praveenkumar, T. Subashini, G.D. Venkatasubbu, T. Prakash, Crystallite size effect on low-dose X-ray sensing behaviour of Y2O3 nanocrystals. Sens. Actuators A **297**, 111544 (2019). https://doi.org/10.1016/j.sna.2019.111544